

Small-signal equivalent circuit for double quantum dots at low-frequencies

Cite as: Appl. Phys. Lett. **114**, 253505 (2019); <https://doi.org/10.1063/1.5098889>

Submitted: 04 April 2019 . Accepted: 12 June 2019 . Published Online: 27 June 2019

M. Esterli, R. M. Otxoa, and M. F. Gonzalez-Zalba



View Online



Export Citation



CrossMark

ARTICLES YOU MAY BE INTERESTED IN

[Electrical property measurement of two-dimensional hole-gas layer on hydrogen-terminated diamond surface in vacuum-gap-gate structure](#)

Applied Physics Letters **114**, 253504 (2019); <https://doi.org/10.1063/1.5099395>

[A high efficiency low-temperature microwave-driven atmospheric pressure plasma jet](#)

Applied Physics Letters **114**, 254106 (2019); <https://doi.org/10.1063/1.5108538>

[Niobium diselenide superconducting photodetectors](#)

Applied Physics Letters **114**, 251103 (2019); <https://doi.org/10.1063/1.5097389>

Applied Physics Letters

Mid-IR and THz frequency combs
special collection

[Read Now!](#)



Small-signal equivalent circuit for double quantum dots at low-frequencies

Cite as: Appl. Phys. Lett. **114**, 253505 (2019); doi: [10.1063/1.5098889](https://doi.org/10.1063/1.5098889)

Submitted: 4 April 2019 · Accepted: 12 June 2019 ·

Published Online: 27 June 2019



View Online



Export Citation



CrossMark

M. Esterli,¹ R. M. Otxoa,^{1,2} and M. F. Gonzalez-Zalba^{1,a)}

AFFILIATIONS

¹Hitachi Cambridge Laboratory, J. J. Thomson Ave., Cambridge CB3 0HE, United Kingdom

²Donostia International Physics Center, Paseo Manuel de Lardizabal 4, Donostia-San Sebastian 20018, Spain

^{a)}E-mail: mg507@cam.ac.uk

ABSTRACT

Due to the quantum nature of current flow in single-electron devices, new physical phenomena can manifest when probed at finite frequencies. Here, we present a semiclassical small-signal model approach to replace complex single-electron devices by parametric circuit components that could be readily used in analog circuit simulators. Our approach is based on weakly driven quantum two-level systems, and here, we use it to calculate the low frequency impedance of a single-electron double quantum dot (DQD). We find that the total impedance is composed of three elements that were previously considered separately: a dissipative term, corresponding to the Sisyphus resistance, and two dispersive terms, composed of the quantum and tunneling capacitance. Finally, we combine the parametric terms to understand the interaction of the DQD with a slow classical electrical oscillator which finds applications in nonresonant state readout of quantum bits and parametric amplification.

Published under license by AIP Publishing. <https://doi.org/10.1063/1.5098889>

Many components of classical electronic circuits, such as the diode or the transistor, present a nonlinear dependence on the current vs voltage. In general, circuits containing these devices do not have simple analytical solutions but can be efficiently approximated using small signal expansion around a bias point when the amplitude of an AC excitation is small compared to the DC signals. This method, known as small-signal modeling, is used in, for example, the design of analog circuits. Single-electron devices, electronic components whose electrical properties are governed by the discreteness of the charge and the effects of quantum confinement, are also nonlinear and hence subject to small-signal modeling. However, several experiments have shown that the AC response of low-dimensional electronic devices may differ from the classical expectations.^{1,2} In the case of zero-dimensional systems, new terms associated with charge relaxation, such as the Sisyphus resistance,^{3,4} with irreversible particle tunneling, such as the tunneling capacitance,^{5–11} and with variations in the chemical potential due to the finite density of states, such as the quantum capacitance,^{12–18} can appear under the appropriate experimental conditions. This raises the question, what does a consolidated small-signal equivalent of a single-electron device look like?

In this letter, we apply a semiclassical small-signal modeling to a prime example of a single-electron device, the single-electron double

quantum dot (DQD). We show now that all the aforementioned circuit components, the Sisyphus resistance and the quantum and tunneling capacitance, manifest simultaneously in the AC response. Both the Sisyphus resistance and the tunneling capacitance arise from irreversible charge relaxation processes that occur when the system is driven at frequencies comparable to or larger than the relaxation rate of the system. The former is linked to phonon pumping processes^{19,20} and leads to net power dissipation. On the other hand, the quantum capacitance appears when reversible charge polarization occurs due to the discrete density of states and the nonlinearity of the energy levels. We combine all these parametric terms in a unified description to replace the DQD by its low-frequency small-signal equivalent circuit. We describe the circuit analytically to understand its dependence on probe frequency, tunnel coupling, relaxation rates, and electron temperature of the system. Finally, we present the single-frequency response of the circuit to help identify experimentally the dissipative and purely dispersive regimes. Our approach can be applied to multilevel quantum systems as long as their Hamiltonian and relaxation rates are known. Moreover, our analysis provides a way to replace complex single-electron devices for their low-frequency equivalent models in the form of parametric resistances and reactances. The

models could be used in circuit simulators, like SPICE,²¹ to design complex quantum analog circuits, in particular for efficient dispersive readout of quantum bits and for parametric amplification.

We consider a closed tunnel-coupled DQD, as schematically depicted in Fig. 1(a). Two dots $i = 1, 2$ are connected to a drive gate electrode (G) via gate capacitances C_{Gi} and to grounded reservoir electrodes at temperature T via C_{Si} . The interdot tunnel barrier has a mutual capacitance, C_m , and tunnel resistance, R_T . The system can be described by an equivalent impedance, Z_{eq} such as $V_G = Z_{eq} I_G$, where V_G and I_G are the gate voltage and the gate current, respectively. In this manuscript, we consider the system driven by a small-amplitude excitation, $V_G = \delta V_G \sin(\omega t)$, where the excitation frequency is much smaller than the DQD frequency $\omega \ll \Delta_c/\hbar$, the rate of transit through the anticrossing is small, and the DQD is weakly coupled to the reservoirs. In this limit, as we shall see later, the DQD impedance is $Z_{eq} = (i\omega C_{total} + 1/R_{Sis})^{-1}$, where C_{total} is the total equivalent capacitance of the system and R_{Sis} is the Sisyphus resistance of the DQD [see Fig. 1(b)].

To obtain an analytical expression of Z_{eq} , we take the definition of the gate current

$$I_G = \frac{d(Q_1 + Q_2)}{dt}, \quad (1)$$

where Q_i is the total charge in the respective quantum dot (QD), which includes the discrete and externally induced charge. We expand the total charge in the DQD as a function of the gate coupling factors $\alpha_i = C_{Gi}/(C_{Si} + C_{Gi})$ and average electron probability distribution in QD i , P_i , in the weak coupling limit $C_m \ll C_{Si} + C_{Gi}$ and obtain

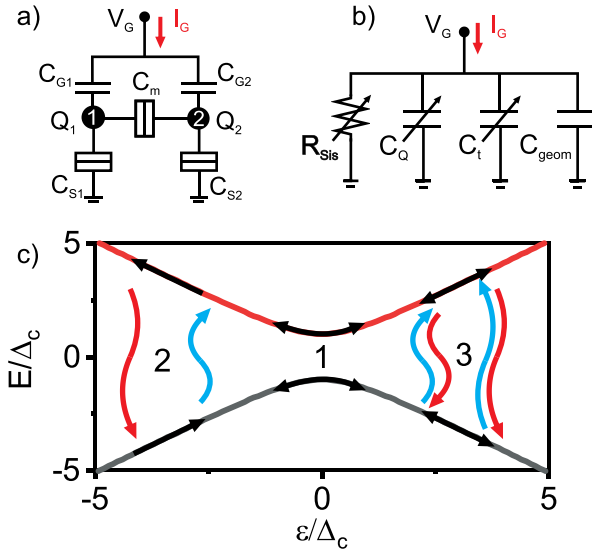


FIG. 1. Double quantum dot equivalent circuit and physical processes. (a) DC equivalent circuit of a DQD. The tunnel barriers, indicated by rectangles, consist of a capacitor in parallel with a resistor. (b) AC small-signal equivalent circuit of the DQD as seen from the gate electrode (G). The arrows indicate parametric impedances. (c) Ground state (gray) and excited state energy (red) of the DQD as a function of reduced detuning. The black arrows indicate the work done by the AC voltage source, and the red and blue wiggly lines indicate phonon emission and absorption. Process associated with quantum capacitance (1) to Sisyphus resistance and tunneling capacitance (2) and purely to tunneling capacitance (3).

$$Q_1 + Q_2 = \sum_i \alpha_i (C_{Si} V_G + e P_i), \quad (2)$$

where e is the charge of the electron. Using Eqs. (1) and (2) for inter-dot charge transitions, $dP_2/dt = -dP_1/dt$, we arrive at

$$I_G = \frac{V_G}{Z_{eq}} = C_{geom} \frac{dV_G}{dt} + e\alpha' \frac{dP_2}{dt}. \quad (3)$$

Here, $C_{geom} = \sum_i \alpha_i C_{Si}$ and $\alpha' = \alpha_2 - \alpha_1$. In Eq. (3), the semi-classical nature of our system becomes apparent. The first term is related to a purely classical reactive term, C_{geom} , which corresponds to the geometrical capacitance of the DQD, whereas the second is linked to changes in electron probability distribution over time. In order to understand the nature of the latter term, we revert to the quantum mechanical description of the DQD. In the single-electron regime, the DQD is described by the Hamiltonian

$$H = -\frac{\Delta_c}{2} \sigma_x - \frac{\varepsilon}{2} \sigma_z, \quad (4)$$

where ε is the energy detuning between quantum dots, Δ_c is the tunnel coupling energy, and $\sigma_{x(z)}$ are the Pauli matrices. We consider the low-frequency regime, $\omega \ll \Delta_c/\hbar$. The corresponding eigenenergies of the system are given by

$$E_{\pm} = \pm \frac{1}{2} \sqrt{\varepsilon^2 + \Delta_c^2}, \quad (5)$$

and the energy difference between the excited and the ground state is $\Delta E = E_+ - E_-$, see Fig. 1(c). At large detunings, the eigenstates coincide with the charge states of the DQD. In general, the probability in the charge basis P_2 can be expressed in terms of the probabilities in the ground state (GS) and excited state (ES) energy basis, P_{\pm} ,

$$P_2 = P_2^- P_- + P_2^+ P_+ = \frac{1}{2} + \frac{\varepsilon}{2\Delta E} (P_- - P_+), \quad (6)$$

since $P_2^{\pm} = (1 \mp \varepsilon/\Delta E)/2$, Ref. 22. If the system is driven at a finite rate, $\varepsilon(t) = \varepsilon_0 + \delta\varepsilon \sin(\omega t)$ and the excitation rate is low $\omega \ll \Delta_c^2/(\hbar\delta\varepsilon)$ to avoid Landau-Zener transitions, an electron can change its probability distribution in the DQD in two different ways:^{22,23} either via adiabatic charge polarization [process 1 in Fig. 1(c) associated with the time derivative of $\varepsilon/\Delta E$] or irreversibly via phonon absorption and emission (processes 2 and 3 associated with the time derivative of $P_- - P_+$). Here, ε_0 is the bias or quiescent point. To calculate the GS and ES probability distribution $P_{-(+)}$, we resort to a master equation formalism

$$\begin{aligned} \dot{P}_- &= \Gamma_- P_+ - \Gamma_+ P_- \\ \dot{P}_+ &= -\Gamma_- P_+ + \Gamma_+ P_-, \end{aligned} \quad (7)$$

where $\Gamma_+ = \Gamma^c n_p$ is the phonon absorption rate and $\Gamma_- = \Gamma^c(1 + n_p)$ is the phonon emission rate. Here, $n_p = [\exp(\Delta E/k_B T) - 1]^{-1}$ is the phonon occupation number and Γ^c is a material-dependent charge relaxation rate. We note that Eq. (7) is applicable as long as $\hbar\Gamma^c \ll k_B T$. We solve Eq. (7) to first order approximation in $\delta\varepsilon/\Delta_c$ (small-signal limit) and obtain the steady-state GS and ES probabilities

$$\begin{aligned} P_{\pm} &= P_{\pm}^0 + \delta P_{\pm} = \frac{e^{\pm \Delta E_0/2k_B T}}{e^{-\Delta E_0/2k_B T} + e^{\Delta E_0/2k_B T}} \\ &\quad \pm \frac{\eta \delta \varepsilon}{\omega^2 + \gamma^2} [\gamma \sin(\omega t) - \omega \cos(\omega t)]. \end{aligned} \quad (8)$$

Here, P_{\pm}^0 are the GS and ES equilibrium probabilities dictated by Boltzmann statistics at the quiescent point, γ is the characteristic rate of relaxation of the system, and η is related to the amplitude of the induced probability oscillations

$$\gamma = \Gamma_-^0 + \Gamma_+^0 = \Gamma^c \coth(\Delta E_0/2k_B T)$$

$$\eta = P_+^0 \frac{\partial \Gamma_-}{\partial \varepsilon} \bigg|_{\varepsilon_0} - P_-^0 \frac{\partial \Gamma_+}{\partial \varepsilon} \bigg|_{\varepsilon_0} = \frac{\gamma}{4k_B T} \frac{\varepsilon_0}{\Delta E_0} \frac{1}{\cosh^2(\Delta E_0/2k_B T)}, \quad (9)$$

where Γ_{\pm}^0 are the relaxation rates at the quiescent point. From Eq. (8), we see that when $\omega \ll \gamma$, P_{\pm} track the probability distribution given by Boltzmann statistics at each instant. However, when $\omega \gg \gamma$, the probability acquires a -90° phase with respect to the excitation and the amplitude of the oscillations is reduced, i.e., the system is unable to track the instantaneous oscillatory input.

Next, we solve Eq. (3) to first order approximation in $\delta\varepsilon/\Delta_c$ and get

$$I_G = \frac{V_G}{Z_{eq}} = C_{geom} \frac{dV_G}{dt} + \frac{(e\alpha')^2}{2} \frac{\Delta_c^2}{(\Delta E_0)^3} \Delta P^0 \frac{dV_G}{dt} + \frac{(e\alpha')^2}{2} \frac{\varepsilon_0}{\Delta E_0} \frac{2\eta\gamma}{\omega^2 + \gamma^2} \frac{dV_G}{dt} + \frac{(e\alpha')^2}{2} \frac{\varepsilon_0}{\Delta E_0} \frac{2\eta\omega^2}{\omega^2 + \gamma^2} V_G, \quad (10)$$

where $\Delta P^0 = P_-^0 - P_+^0 = \tanh(\Delta E_0/2k_B T)$ is the equilibrium energy polarization. From Eq. (10), we find the analytical expression for Z_{eq} . Terms linear in dV_G/dt are capacitances, whereas the term linear in V_G is linked to resistance. The reactive terms correspond to C_{total} , the sum of the geometrical capacitance, the quantum capacitance

$$\alpha' = 1 \quad C_Q = \frac{(e\alpha')^2}{2} \frac{\Delta_c^2}{(\Delta E_0)^3} \Delta P^0, \quad (11)$$

tunneling

and the tunneling capacitance

$$C_t = \frac{(e\alpha')^2}{2} \frac{1}{2k_B T} \left(\frac{\varepsilon_0}{\Delta E_0} \right)^2 \frac{\gamma^2}{\omega^2 + \gamma^2} \cosh^{-2}(\Delta E_0/2k_B T). \quad (12)$$

limit for $T \rightarrow 0$?

The dissipative term, which appears in parallel, is the Sisyphus resistance

$$R_{Sis} = \frac{4R_Q k_B T}{\alpha'^2 h\gamma} \left(\frac{\Delta E_0}{\varepsilon_0} \right)^2 \frac{\omega^2 + \gamma^2}{\omega^2} \cosh^2(\Delta E_0/2k_B T). \quad (13)$$

limit for $T=0$?

Note that R_Q is the resistance quantum h/e^2 and is related to the resistance of the interdot tunnel barrier, $R_T = 2R_Q k_B T/h\Gamma_0$, Ref. 4.

Next, we investigate the functional dependence of these different circuit components. We start with the Sisyphus resistance. In Fig. 2(a), we plot R_Q/R_{Sis} as a function of detuning for several temperatures. We see that dissipation, which is proportional to R_{Sis}^{-1} , presents two symmetric maxima at finite detuning, whereas dissipation drops to zero at $\varepsilon_0 = 0$ and $|\varepsilon_0| \gg \Delta_c$. Additionally, we observe that dissipation increases as the temperature increases. In Fig. 2(b), we fix the operation frequency to $\omega = \omega_0$ and plot the dependence of R_Q/R_{Sis} with γ . We see that the dissipation presents a maximum at $\gamma/\omega_0 = 1$ and it

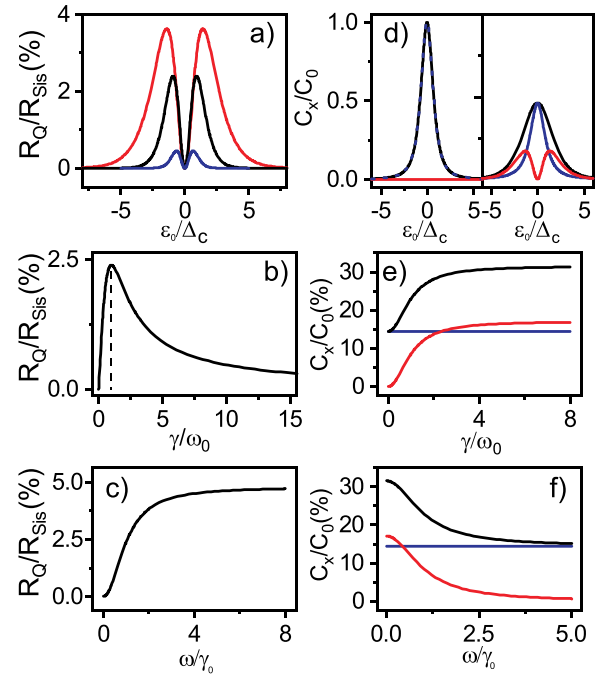


FIG. 2. Parametric impedances. (a) Normalized inverse of the Sisyphus resistance vs reduced detuning for $k_B T/\Delta_c = 0.25, 0.5$ and 1 (blue, black, and red traces, respectively) and $\Gamma^c = \omega$ in percentage. (b) R_Q/R_{Sis} as a function of reduced relaxation rate and (c) as a function of reduced operation frequency for $k_B T/\Delta_c = 0.5$ and $\varepsilon_0/\Delta_c = 1$. (d) Normalized parametric (black), quantum (blue), and tunneling capacitance (red) C_x/C_0 as a function of reduced detuning for $k_B T/\Delta_c = 0.01$ and 1 (left and right panels, respectively) and $\Gamma^c/\omega = 10$. $C_0 = (e\alpha')^2/2\Delta_c$, and we set $\alpha' = 1$. C_x/C_0 as a function of reduced relaxation rate (e) and operation frequency (f) for $k_B T/\Delta_c = 1$ and $\varepsilon_0/\Delta_c = 1$ in percentage.

tends to zero when $\gamma/\omega_0 \rightarrow 0$ and ∞ . Finally, we fix the characteristic relaxation rate to $\gamma = \gamma_0$ and plot R_Q/R_{Sis} as a function of ω in Fig. 2(c). We see that dissipation increases as $\omega \gg \gamma_0$ until it saturates. Although dissipation in each cycle decreases, the overall dissipation tends to a constant value because the increased number of cycles matches the reduction of energy dissipation per cycle.

As depicted in process 2 in Fig. 1(c), phonon pumping drives the mechanism. In the first part of the cycle, the system can be excited via phonon absorption. If the relaxation occurs on the time scale of the drive, it can occur at a substantially different point in detuning, leading to the emission of a phonon with larger energy than the one absorbed, resulting in net power dissipation. At large detunings, the cycle cannot be completed because the energy of the phonon necessary to produce an excitation becomes large compared to the thermal energy. At zero detuning, the energies of the absorbed and emitted phonons are on average the same, resulting in no net power dissipation. The Sisyphus cycle has been observed in single-electron boxes and single QDs and corresponds to Sisyphus heating where energy is transferred from the voltage source to the system^{3,4} but is yet to be observed in DQDs. Since phonon pumping is driven by the number of phonons in the environment, n_p , the increase in the temperature leads to enhanced dissipation. In contrast, if the relaxation is much slower, the system will not be excited (process 1), or if it is much faster, the cycle will be

$$\cosh^2 \frac{\Delta E_0}{k_B T} \xrightarrow{T \rightarrow 0} \cosh^2(\infty) = \infty$$

cosh(x)

$\frac{e^x + e^{-x}}{2}$

done adiabatically following thermal equilibrium (process 3). In both cases, the processes are adiabatic; however, there is a subtle difference between them. In process 1, the probabilities remain constant during the cycle. It is therefore an isentropic and hence reversible process. In process 3, since the system is in thermal equilibrium, there is maximal entropy production, and hence, the process is irreversible.

Now, we move on to the study of the reactive terms. We focus on the parametric terms, the quantum and tunneling capacitance and its sum, the parametric capacitance, C_{par} . In Fig. 2(d), we plot both as a function of detuning for the low-temperature limit $k_B T/\Delta_c = 0.01$ and the high-temperature limit $k_B T/\Delta_c = 1$ (left and right panels, respectively). In the low- T limit, the parametric capacitance (black) consists of a single peak centered at $\varepsilon_0 = 0$ and contains exclusive contributions from the quantum capacitance (dashed blue). In the high- T regime, the parametric capacitance (black) equally presents a single peak, although of reduced height due to the reduced equilibrium energy polarization. However, the peak now consists of contributions from both C_Q and C_t in blue and red, respectively. The line shape of C_t coincides with that of R_Q/R_{sis} indicating that the same mechanism, phonon pumping, drives the process. However, when we explore the dependence of the capacitance with γ and ω , we observe subtle differences. In Figs. 2(e) and 2(f), we see that C_Q (blue) does not depend on the drive frequency. It is exclusively determined by the nonlinear nature of the energy levels, see Eq. (6). On the other hand, C_t (red) and hence C_{par} increase with increasing γ/ω in a symmetric way. In Fig. 2(e), we fix the resonant frequency and change γ , whereas in Fig. 2(f), we fix γ and change the frequency. With these three plots, we can get a comprehensive picture of the dispersive response. The quantum capacitance is linked to isentropic charge polarization due to the nonlinearity of the energy levels, whereas the tunneling capacitance is linked to thermal probability redistribution (maximal entropy production). The latter depends strongly on the system dynamics, i.e., it only manifests when γ is comparable to or larger than ω , this is when tunneling occurs either nonadiabatically (as in the case of the Sisyphus heating) or adiabatically.

We move on to study the response at a single frequency where a combination of these terms can manifest. As we have learned before, R_{sis} and C_t appear when the relaxation rates of the system are comparable to or larger than the probe frequency. For single-electron DQDs with typical charge relaxation rates in the 0.01–10 GHz regime,^{24,25} probing those terms involves using radiofrequency (RF) or microwave (MW) excitation. To guide experiments in which the regimes 1, 2, and 3 in Fig. 1(c) could be observed, we suggest embedding the DQD in a resonator. In this example, we select a tank LC resonator and simulate its reflection coefficient when probed at its resonant frequency $\omega_0 = 1/\sqrt{LC}$, see Fig. 3(a). In particular, we present the normalized phase shift of the resonator $\Delta\varphi/\varphi^0$. In Fig. 3(b), we plot $\Delta\varphi/\varphi^0$ as a function of detuning for different temperatures. At low temperatures $k_B T/\Delta_c = 0.1$ (blue trace), the phase response is composed of a single dip whose line shape coincides with that of C_Q . It corresponds to the expectation that when an overcoupled resonator is subject to a purely capacitive signal ΔC , it produces a phase change such as $\Delta\varphi = -2Q\Delta C/C$ as long as $Q^{-1} > \Delta C/2C$ (Q is the quality factor of the resonator). When the temperature increases to $k_B T/\Delta_c = 1.5$ and 2.5 (black and red traces, respectively), the line shape evolves to a double dip with a local maximum at $\varepsilon_0 = 0$. For these plots, we select $\Gamma^c/\omega_0 = 1$ to maximize the effect of the Sisyphus resistance.

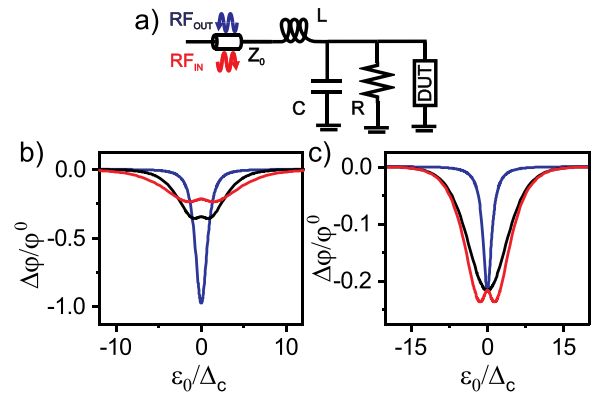


FIG. 3. Single-frequency response in a resonator. (a) Schematic of the LC resonator used for the simulations: $Z_0 = 50 \, \Omega$, $L = 405 \, \text{nH}$, $R = 20 \, \text{k}\Omega$, and $C = 0.53 \, \text{pF}$. We replace the device under test (DUT) by the circuit equivalent in Fig. 1(b). Reduced reflected phase shift as a function of reduced detuning for variable temperature (b) and relaxation rate (c). In (b), $\Gamma^c/\omega_0 = 1$ and $k_B T/\Delta_c = 0.1, 1.5$, and 2.5 (blue, black, and red, respectively). In (c), $k_B T/\Delta_c = 2.5$ and $\Gamma^c/\omega_0 = 0, 1$, and 100 (blue, red, and black, respectively). $\varphi^0 = 0.2 \, \text{rad}$.

Next, in Fig. 3(c), we show $\Delta\varphi/\varphi^0$ as a function of detuning for different relaxation rates. The blue and black traces show the slow and fast relaxation regimes, $\Gamma^c/\omega_0 = 0$ and 100, respectively. Both situations carry a purely capacitive signal and hence present a single dip centered at $\varepsilon_0 = 0$. The blue trace has contributions exclusively from C_Q as the system has no time to reach instantaneous thermal equilibrium on the time scale of the drive, whereas for the black trace, the rates are sufficiently fast to be in thermal equilibrium, and hence, the trace combines the quantum and tunneling capacitance. In the case of intermediate relaxation $\Gamma^c/\omega_0 = 1$ (red trace), we again observe the double dip line shape, a signature of Sisyphus dissipation where nonadiabatic transitions take place. Overall, these plots allow us to identify the set of parameters where the three distinct regimes could be observed by measurements. For process 1, where only C_Q contribute to the signal, low temperature and/or slow relaxation is required. For process 3, where both C_Q and C_t contribute, high temperatures and fast relaxation are required. Ultimately, for the nonadiabatic regime where Sisyphus processes occur (process 2), high temperatures and a frequency that matches the relaxation rate are necessary. In this regime, to describe the effect of the device on the resonator, all terms, C_Q , C_t , as well as R_{sis} , need to be taken into account.

In conclusion, we have developed a semiclassical framework to understand the low-frequency response of a DQD system in the small-signal regime. The mapping of complex single-electron devices on to conventional circuit elements will be a valuable tool to generate device models for analog quantum circuit simulation, and it will be applicable to dispersive radio frequency readout currently used in solid-state devices^{26–28} as well as parametric amplification.^{29–31}

We acknowledge useful discussions with Andras Pályi and James Haigh. This research received funding from the European Union's Horizon 2020 Research and Innovation Programme under Grant agreement No. 688539 (<http://mos-quito.eu>), the Winton Programme of the Physics of Sustainability, and the Erasmus+ Programme. The participation of M.E. has been carried out within the framework Agreement No. UAM-SRUK 2018.

REFERENCES

- ¹M. Büttiker, H. Thomas, and A. Prêtre, "Mesoscopic capacitors," *Phys. Lett. A* **180**(4), 364–369 (1993).
- ²J. Gabelli, G. Fève, J.-M. Berroir, B. Plaçais, A. Cavanna, B. Etienne, Y. Jin, and D. C. Glattli, "Violation of Kirchhoff's laws for a coherent RC circuit," *Science* **313**(5786), 499–502 (2006).
- ³F. Persson, C. M. Wilson, M. Sandberg, and P. Delsing, "Fast readout of a single cooper-pair box using its quantum capacitance," *Phys. Rev. B* **82**, 134533 (2010).
- ⁴M. F. Gonzalez-Zalba, S. Barraud, A. J. Ferguson, and A. C. Betz, "Probing the limits of gate-based charge sensing," *Nat. Commun.* **6**, 6084 (2015).
- ⁵R. C. Ashoori, H. L. Stormer, J. S. Weiner, L. N. Pfeiffer, S. J. Pearton, K. W. Baldwin, and K. W. West, "Single-electron capacitance spectroscopy of discrete quantum levels," *Phys. Rev. Lett.* **68**, 3088–3091 (1992).
- ⁶R. C. Ashoori, H. L. Stormer, J. S. Weiner, L. N. Pfeiffer, K. W. Baldwin, and K. W. West, "N-electron ground state energies of a quantum dot in magnetic field," *Phys. Rev. Lett.* **71**, 613–616 (1993).
- ⁷C. Ciccarelli and A. J. Ferguson, "Impedance of the single-electron transistor at radio-frequencies," *New J. Phys.* **13**, 093015 (2011).
- ⁸S. J. Chorley, J. Wabnig, Z. V. Penfold-Fitch, K. D. Petersson, J. Frake, C. G. Smith, and M. R. Buitelaar, "Measuring the complex admittance of a carbon nanotube double quantum dot," *Phys. Rev. Lett.* **108**, 036802 (2012).
- ⁹M. D. Schroer, M. Jung, K. D. Petersson, and J. R. Petta, "Radio frequency charge parity meter," *Phys. Rev. Lett.* **109**, 166804 (2012).
- ¹⁰M. G. House, K. Kobayashi, B. Weber, S. J. Hile, T. F. Watson, J. van der Heijden, S. Rogge, and M. Y. Simmons, "Radio frequency measurements of tunnel couplings and singlet-triplet spin states in Si:P quantum dots," *Nat. Commun.* **6**, 8848 (2015).
- ¹¹R. Mizuta, R. M. Otxoa, A. C. Betz, and M. F. Gonzalez-Zalba, "Quantum and tunneling capacitance in charge and spin qubits," *Phys. Rev. B* **95**, 045414 (2017).
- ¹²S. Luryi, "Quantum capacitance devices," *Appl. Phys. Lett.* **52**(6), 501–503 (1988).
- ¹³T. Duty, G. Johansson, K. Bladh, D. Gunnarsson, C. Wilson, and P. Delsing, "Observation of quantum capacitance in the cooper-pair transistor," *Phys. Rev. Lett.* **95**, 206807 (2005).
- ¹⁴M. A. Sillanpää, T. Lehtinen, A. Paila, Yu. Makhlin, L. Roschier, and P. J. Hakonen, "Direct observation of Josephson capacitance," *Phys. Rev. Lett.* **95**, 206806 (2005).
- ¹⁵K. D. Petersson, C. G. Smith, D. Anderson, P. Atkinson, G. A. C. Jones, and D. A. Ritchie, "Charge and spin state readout of a double quantum dot coupled to a resonator," *Nano Lett.* **10**, 2789–2793 (2010).
- ¹⁶A. Cottet, C. Mora, and T. Kontos, "Mesoscopic admittance of a double quantum dot," *Phys. Rev. B* **83**, 121311 (2011).
- ¹⁷J. I. Colless, A. C. Mahoney, J. M. Hornibrook, A. C. Doherty, H. Lu, A. C. Gossard, and D. J. Reilly, "Dispersive readout of a few-electron double quantum dot with fast rf gate sensors," *Phys. Rev. Lett.* **110**, 046805 (2013).
- ¹⁸A. C. Betz, R. Wacquez, M. Vinet, X. Jehl, A. L. Saraiva, M. Sanquer, A. J. Ferguson, and M. F. Gonzalez-Zalba, "Dispersively detected pauli spin-blockade in a silicon nanowire field-effect transistor," *Nano Lett.* **15**(7), 4622–4627 (2015).
- ¹⁹K.-H. Ahn and P. Mohanty, "Quantum friction of micromechanical resonators at low temperatures," *Phys. Rev. Lett.* **90**, 085504 (2003).
- ²⁰M. Grajcar, S. H. W. van der Ploeg, A. Izmalkov, E. Il'ichev, H.-G. Meyer, A. Fedorov, A. Shnirman, and G. Schön, "Sisyphus cooling and amplification by a superconducting qubit," *Nat. Phys.* **4**, 612 (2008).
- ²¹Simulation program with Integrated Circuit Emphasis.
- ²²M. F. Gonzalez-Zalba, S. N. Shevchenko, S. Barraud, J. R. Johansson, A. J. Ferguson, F. Nori, and A. C. Betz, "Gate-sensing coherent charge oscillations in a silicon field-effect transistor," *Nano Lett.* **16**, 1614 (2016).
- ²³S. N. Shevchenko, S. Ashhab, and F. Nori, "Landau-Zener-Stückelberg interferometry," *Phys. Rep.* **492**(1), 1–30 (2010).
- ²⁴E. Dupont-Ferrier, B. Roche, B. Voisin, X. Jehl, R. Wacquez, M. Vinet, M. Sanquer, and S. De Franceschi, "Coherent coupling of two dopants in a silicon nanowire probed by Landau-Zener-Stückelberg interferometry," *Phys. Rev. Lett.* **110**, 136802 (2013).
- ²⁵P. Scarlino, D. J. van Woerkom, A. Stockklauser, J. V. Koski, M. C. Collodo, S. Gasparinetti, C. Reichl, W. Wegshneider, T. Ihn, K. Ensslin, and W. Wallraff, "All-microwave control and dispersive readout of gate-defined quantum dot qubits in circuit quantum electrodynamics," *PRL* **122**, 206802 (2019).
- ²⁶P. Pakkiam, A. V. Timofeev, M. G. House, M. R. Hogg, T. Kobayashi, M. Koch, S. Rogge, and M. Y. Simmons, "Single-shot single-gate rf spin readout in silicon," *Phys. Rev. X* **8**, 041032 (2018).
- ²⁷A. West, B. Hensen, A. Jouan, T. Tanttu, C. H. Yang, A. Rossi, M. F. Gonzalez-Zalba, F. E. Hudson, A. Morello, D. J. Reilly, and A. S. Dzurak, "Gate-based single-shot readout of spins in silicon," *Nat. Nanotechnol.* **14**, 437 (2019).
- ²⁸A. Crippa, R. Ezzouch, A. Aprá, L. Hutin, B. Bertrand, M. Vinet, M. Urdampilleta, T. Meunier, M. Sanquer, X. Jehl, R. Maurand, and S. De Franceschi, "Gate-reflectometry dispersive readout of a spin qubit in silicon," preprint [arXiv:1811.04414](https://arxiv.org/abs/1811.04414) (2018).
- ²⁹A. Roy and M. Devoret, "Introduction to parametric amplification of quantum signals with Josephson circuits," *C. R. Phys.* **17**(7), 740–755 (2016).
- ³⁰J. Stehlik, Y.-Y. Liu, C. M. Quintana, C. Eichler, T. R. Hartke, and J. R. Petta, "Fast charge sensing of a cavity-coupled double quantum dot using a Josephson parametric amplifier," *Phys. Rev. Appl.* **4**, 014018 (2015).
- ³¹C. Macklin, K. O'Brien, D. Hover, M. E. Schwartz, V. Bolkhovskiy, X. Zhang, W. D. Oliver, and I. Siddiqi, "A near-quantum-limited Josephson traveling-wave parametric amplifier," *Science* **350**(6258), 307–310 (2015).